

“This document is the Accepted Manuscript version of a Published Work that appeared in final form in **Analytical Chemistry**, copyright © American Chemical Society after peer review and technical editing by the publisher. To access the final edited and published work see [<https://pubs.acs.org/doi/10.1021/acs.analchem.6b00665>].”

## Biospectroscopy of nanodiamond-induced toxicity in liver cells – a nanoIR study

Dipesh Khanal,<sup>†</sup> Alexey Kondyurin,<sup>‡</sup> Herman Hau,<sup>†</sup> Jonathan C. Knowles,<sup>‡</sup> Olga Levinson,<sup>§</sup> Iqbal Ramzan,<sup>†</sup> Dong Fu,<sup>†</sup> Curtis Marcott,<sup>§</sup> Wojciech Chrzanowski<sup>\*,†, i</sup>

<sup>†</sup>Faculty of Pharmacy, The University of Sydney, NSW 2006, Australia

<sup>‡</sup>School of Physics, The University of Sydney, NSW 2006, Australia

<sup>§</sup>Light Light Solutions, P. O. Box 81486, Athens, GA 30608-1484, USA

<sup>‡</sup>Division of Biomaterials and Tissue Engineering, UCL Eastman Dental Institute, University College London, London, UK

<sup>§</sup>Ray Techniques Ltd., Jerusalem, 9139101, Israel

<sup>i</sup>Australian Institute of Nanoscale Science and Technology, The University of Sydney, NSW 2006, Australia

**ABSTRACT:** The toxicity of nanomaterials raises major concerns because of the impact that nanomaterials may have on health, which remains poorly understood. We ought to explore the fate of individual nanoparticles in cells at nano/molecular levels to establish their safety profiles. Conformational changes in secondary protein structures are one of the main indicators that suggest impaired biological function and hence, the ability to identify these changes at a nanoscale offers unique insights into the nanotoxicity of materials. Here, we used nanoscale Infrared spectroscopy and demonstrated for the first time that nanodiamonds induced alterations in both extra and intracellular secondary protein structures, leading to the formation of antiparallel  $\beta$ -sheet,  $\beta$ -turns, intermolecular  $\beta$ -sheet and aggregation of proteins. These protein conformational changes may result in the loss of functionality of proteins and in turn lead to adverse effects.

### INTRODUCTION

Nanomaterials, which are present virtually everywhere in cosmetics, toiletries, food products, medical imaging systems and therapeutics<sup>1-5</sup>, raises colossal and increasing safety concerns. As highlighted by a number of studies, nanoparticles are readily taken up by cells through different active or passive pathways, primarily via phagocytosis, pinocytosis and endocytosis<sup>6-9</sup>. However, the mechanisms and pathways involved in the uptake of different types of nanoparticles are complex and may be dependent

on a number of factors such as their size<sup>10,11</sup>, surface chemistry, charge, geometry or shape<sup>11-13</sup>, and also vary from cell to cell<sup>14-16</sup>. The disparity in properties and uptake mechanisms affects the localization of these nanoparticles and interactions with cells and tissues. Therefore, there is a pressing need to explore the fate of individual nanoparticles at the cellular and molecular level.

Interactions between nanoparticles and cells are highly dependent on nanoparticle–protein or nanoparticle–macromolecule interactions. Proteins could be in the form of structural proteins (e.g. tubulin, actin), cell signaling molecules (e.g. hormones) or even enzymes. Slight changes in the conformation of these proteins may lead to alteration or even complete loss of their functionality. It is well documented that nanoparticles have high affinity to proteins, which depends on their physicochemical properties including size, charge and shape<sup>17</sup>. Nanoparticle–protein interactions may result in changes in the conformation of proteins<sup>18,19</sup>. For instance, Quantum dots have been reported to induce significant decrease in  $\alpha$ -helical content of human adult hemoglobin<sup>20</sup>. Similarly, gold and polystyrene particles lead to decreased  $\alpha$ -helix

and increased  $\beta$ -turn structures in bovine serum albumin<sup>18,21</sup>. It is thus evident that we need to explore how nanoparticle-cell interactions may disrupt protein conformations. Nanoparticles and proteins have comparable sizes, and thus may interfere with the cell signaling processes or impair protein function. In addition, these nanoparticles may inadvertently be involved in chaperone-like activity, which is vital for controlling protein folding during their assembly. This means that interference of protein folding by nanoparticles may lead to the formation of peptide aggregates or peptide fibrils that have amyloid-like structures<sup>19,22</sup>, which are known to be linked to neurodegenerative diseases such as Alzheimer's disease<sup>19,22</sup>. Biospectroscopic studies involve the use of non-invasive techniques to detect the effect of nanoparticles on intracellular proteins at a macro-micron level<sup>23</sup>. Raman spectroscopy<sup>24,25</sup>, Fourier transform infrared spectroscopy (FTIR), circular dichroism spectroscopy, surface plasmon resonance and X-ray crystallography<sup>18,26-28</sup> are some of the traditionally used techniques to investigate the effect of particles on protein conformation. However, all these techniques have limited sensitivity and resolution. The micron-level resolution may not provide sufficiently detailed information on the effect of nanoparticles on cellular proteins. For example, the lateral resolution of the FTIR technique ranges up to 24  $\mu\text{m}$ <sup>29</sup> in the mid-IR range which is much too large to identify the subtle differences or changes resulting from interactions between individual nanoparticles and proteins at a nanoscale<sup>30,31</sup>. In addition, FTIR spectra collected from the bulk material may not actually represent the chemical fingerprint of the sample at the nano level.

Recently, Dazzi<sup>32-34</sup> developed the atomic force microscopy infrared spectroscopy (AFM-IR, aka nanoIR), which is based on photothermally induced resonance and is currently the most sensitive technique to

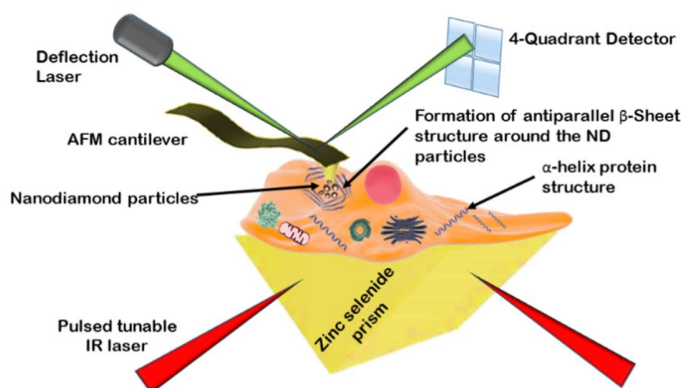


**Figure 1.** Schematic representation of AFM-IR spectroscopy: conformational changes in the protein structure occurred after exposure to nanodiamond particles. Formation of antiparallel  $\beta$ -sheet was detected around the region of nanoparticle localization whereas non treated cells had high  $\alpha$ -helical content.

measure chemical composition with resolution of <20 nm. This technique may offer tremendous potential to explore the conformational changes of cell proteins in the area surrounding internalized nanoparticles.

In nanoIR, a sample is placed on a transparent, total internal reflective surface e.g. zinc selenide, which is illuminated by a pulsed and tunable IR laser. If the evanescent field excites molecular vibrations in the sample, a small thermal expansion is induced. This expansion results in the oscillation of the AFM cantilever, which serves as a near field detector. The resultant cantilever oscillations are sensed by a four-quadrant detector (Figure 1). These oscillations are recorded as a cantilever ringdown signal. Fourier transformation of this signal generates the signal amplitude corresponding to the IR-absorption<sup>31-36</sup>. Furthermore, the resonant frequency of these oscillations indicates the nanomechanical stiffness of the sample. This can help in identifying the nanoparticles, which typically have a different stiffness to biological structures. In addition, the technique offers lateral resolution in the range of 10 nm to 50 nm<sup>31, 36</sup>. These features make nano-IR a valuable tool for investigating nanoparticle–cell or nanoparticle–protein interactions at their interface.

Nanoscale sp<sup>3</sup> carbon based nanomaterial<sup>37</sup> i.e. nanodiamonds (NDs) is one of the most explored carbon based nanoparticles in recent years. It retains the unique properties of bulk diamonds at nanoscale, which attributes towards its hardness and Young's modulus, optical and fluorescence properties, high thermal conductivity, electrical resistivity and chemical stability<sup>38,39</sup>. Owing to its properties NDs have been used in a wide variety of applications such as magnetic resonance imaging<sup>40</sup>, chromatography<sup>41,42</sup>, mass spectrometry<sup>43</sup>, tribology and lubrication<sup>44</sup>, nanocomposites<sup>45,46</sup>, surgical implants and tissue scaffolds<sup>47</sup>, biomedical imaging and drug delivery<sup>1,48-50</sup>. Detonation technique, laser ablation, high energy ball milling at high pressure and temperature, plasma assisted chemical vapour deposition, autoclave synthesis from supercritical fluids and chlorination of carbides are some of the commonly used manufacturing approaches<sup>38</sup>. The broad application of NDs, compounded with differing manufacturing techniques must raise concerns of increased and variable human and environmental exposure to these nanomaterials. In addition, some studies have highlighted that NDs can induce conformational changes in protein structures but this was confirmed only at macro and micro level. It was found that when bovine serum albumin was exposed to NDs,  $\alpha$ -helical content decreased and  $\beta$ -turn and  $\beta$ -sheet structures increased<sup>28</sup>. It was also shown that the smaller the size (5 nm vs. 50 nm) of the ND, the greater the effect on conformation changes (the loss of functionality) of lysozyme<sup>26,27</sup>. Similarly, Svetlakova *et. al.* reported that ND induces conformational changes in human serum albumin with the cleavage of disulfide bridges, modification of H-bond in tyrosine residues and increase in random coil formation<sup>51</sup>. Given their applications in the biomedical field, precise understanding of how these and other nanoparticles interact with biological systems is vital to assure patient safety.

In this study we focus solely on the investigations of the impact of NDs (model nanoparticle) on the conformation of intracellular proteins (proteins inside liver cell) and extracellular protein (fibronectin-FN) using AFM-IR spectroscopy technique. Since the liver is the primary site of nanoparticle uptake and localization, the investigation of the effect of NDs on liver cells may possibly highlight their impact on overall health. In addition, nanoscale characterization of cellular protein structures after uptake of nanoparticles would provide deeper understanding of the potential of protein denaturation. We demonstrated that NDs induced conformational changes in both extracellular and intracellular proteins. Increased  $\beta$ -sheet content and possible denaturation of proteins were observed after the exposure of intra and extracellular proteins to the NDs.

## EXPERIMENTAL SECTION

### MATERIALS

Rat hepatoma (Fao cell) (donated by Dr. Irwin Arias, National Institutes of Health, USA) cultured in Dulbecco's Modified Eagle's Medium (DMEM) supplemented with 4500 mg/L D-glucose, 2mM L-glutamine (Sigma-Aldrich, Australia), Penstrep® (100 IU mL<sup>-1</sup> penicillin, 100 µg.mL<sup>-1</sup> streptomycin: Gibco, Life Technologies, USA) and 10% Fetal Bovine Serum (Sera Laboratories, UK ) was used to prepare both 2D and 3D liver cell culture models.

### Physico-chemical Characterization

Nanodiamond (ND) produced by laser assisted technology<sup>52</sup> with mean size of 4-5 nm (Ray Techniques Ltd, Israel) were used in the study. Physicochemical properties of ND were characterized with Fourier transform infrared spectroscopy (FTIR), X-ray diffractometry (XRD), atomic force microscopy (AFM), transmission electron microscopy (TEM) and X-ray photoelectron spectroscopy (XPS).

**The crystallinity** of ND was determined by XRD (D8 Advance, Bruker diffractometer- Bruker, UK) in a flat plate geometry using Ni-filtered Cu K $\alpha$  radiation and a Bruker Lynx eye detector. The X-ray diffraction patterns were acquired from 10 to 200° 2 $\theta$  with a step size of 0.02° and a count time of 0.1s.

**Size and morphology** of the ND were assessed with TEM (Philips CM 120- Biofilter, The Netherlands) and AFM (nanoIR, Anasys Instruments, USA). For the AFM studies, ND was first immobilised on freshly cleaved mica functionalised with poly-L-lysine and scanned in AC mode using a silicon nitride cantilever with a spring constant of 40 Nm<sup>-1</sup> (EXT125, AppNano, Mountain View, CA, USA) at a scan rate of 0.50 Hz. The images were processed using the Analysistudio™ software (Anasys Instruments, USA).

**Chemical composition** of ND particles was characterized using XPS (Axis ultra XPS/ESCA–Kratos Analytical, UK) using an Al-K $\alpha$  monochromator X-ray source. Survey scan was acquired at 100 eV pass energy between 0 and 1400 eV. High resolution spectra for carbon, oxygen and nitrogen were collected at 20 eV pass energy. The elemental composition (atomic concentration) was calculated from the high resolution spectra using CasaXPS. The measurements were done in triplicate.

FTIR ATR spectra (bulk measurement of chemical functionality) of the nanodiamond powder were collected by the attenuated total reflectance (ATR) technique on a FTIR7000 series spectrometer (Digilab, USA) with Germanium ATR crystal of 45 degrees incident angle and global source of IR irradiation. Absorbance spectra were acquired in mid IR (infrared) range from 4000 to 400 cm<sup>-1</sup> taking average of 500 scans and an instrumental resolution of 4 cm<sup>-1</sup>.

**Magnetic printing of 3D cell culture model;** to investigate the toxicity of ND, fabrication of 3D models, spheroids, was done using previously published methodology<sup>48,53,54</sup>. Briefly, cell were first incubated with magnetic nanoparticles (Nanoshuttle® (NS), n3D Bioscience, USA) at a concentration of 8 µL.cm<sup>-2</sup> overnight and then levitated magnetically overnight to obtain 3D cellular aggregates. Next, cell aggregates were dispersed and biopatterned into 3D spheroids using magnetic pin drives (Figure S1).

### Viability of cells

Fao cells cultured in 2D monolayer were treated with ND at the concentration of 10, 25, 50 and 100 µg.mL<sup>-1</sup> over the period of 48 h. Viability of cells exposed to ND were assessed using Cell Counting Kit-8 (CCK-8) (Dojindo Molecular Technologies, Inc., Santa Clara, CA) as per manufacturers' protocols. In addition,

viability of cells within the bioprinted spheroids after treatment with ND at a concentration of  $25 \mu\text{g.mL}^{-1}$  for 24 h was evaluated using live/dead assay (PromoCell, Germany) as per the manufacturer's protocol.

## **BIOSPECTROSCOPY – AFM-IR**

**AFM-IR – intracellular protein analysis – sample preparation;** for the investigation of intracellular protein analysis, spheroids treated with ND at a concentration of  $25 \mu\text{g.mL}^{-1}$  were used. As a control, cell spheroid treated with nanoshuttles only and Fao cell pellet obtained after centrifugation of cells cultured in monolayer up to 80% confluency were used.

ND treated spheroid, nanoshuttle loaded spheroids and control cell pellet were fixed in 2.5% glutaraldehyde in 0.1 M phosphate buffer (pH 7.4) for 30 minutes and dehydrated in ethanol (30-100%). Dehydrated spheroids and cell pellet were embedded in Spurr's resin (ProScitech, Australia). Resin-embedded samples were microtomed using glass knives (UltraCut S, Leica Microsystem GmbH, Vienna, Austria) to obtain a semi thin (500 nm) sections. Next the sections were transferred to zinc selenide prisms for biospectroscopic analysis – nanoIR.

**AFM-IR – extracellular protein analysis – sample preparation;** human plasma fibronectin (FN) (>95% purity, Sigma Aldrich) was reconstituted and was diluted to  $20 \mu\text{g.mL}^{-1}$  solution in deionised water. The ND–FN sample were prepared by adding 150  $\mu\text{L}$  of  $1\text{mg.mL}^{-1}$  ND dispersion in deionised water to 1.5 mL of  $20 \mu\text{g.mL}^{-1}$  FN solution. The ND dispersion was sonicated for 1 h using an ultrasonic probe before being added to the protein solution. The ND–FN solution was mixed at  $25^{\circ}\text{C}$  using a vortex mixer for 2 h. Next the solution was centrifuged at 13000 rpm at  $4^{\circ}\text{C}$  for 15 min. Ten  $\mu\text{L}$  of supernatant was transferred to the zinc selenide prism to investigate conformational changes in non-adsorbed protein. The remaining supernatant was removed and the protein–ND pellet was rinsed with deionised water three times followed by centrifugation to remove free proteins. The pellet was redispersed in deionised water and then transferred to the zinc selenide prism and dried under nitrogen gas. The sample was stored in a desiccator to remove the adsorbed moisture prior to AFM-IR measurements. Control pristine fibronectin sample ( $20 \mu\text{g.mL}^{-1}$ ) and FN supernatant were transferred to the zinc selenide prism and dried under the nitrogen gas followed by desiccation prior to the spectra acquisition.

**Nanoscale infrared biospectroscopy** was done using nanoIR (Anasys instruments, USA). Prior to the acquisition of the spectra, four IR background spectra were collected from 1000 to  $1800 \text{ cm}^{-1}$ . These spectra were averaged and normalized to calibrate the signal intensity as a function of wavenumber. Second mode of cantilever oscillation was chosen for optimizing the cantilever ringdown signal at a frequency centre of 185 kHz with a frequency window of 20 kHz. The infrared laser was optimized at  $1550 \text{ cm}^{-1}$ ,  $1620 \text{ cm}^{-1}$ ,  $1640 \text{ cm}^{-1}$ ,  $1690 \text{ cm}^{-1}$  and  $1723 \text{ cm}^{-1}$  for cell-based samples (ND-treated spheroid sections, NS treated spheroid and control cell sections) as well as for extracellular protein-based samples (FN, FN–ND and FN supernatant). Co-averages of 256 were used for optimization. Laser power was adjusted to obtain a clean and distinct 'IR-hotspot' in the centre (Figure S5).

AFM-IR spectra were collected from  $1300 \text{ cm}^{-1}$  to  $1800 \text{ cm}^{-1}$  at  $1 \text{ cm}^{-1}$  interval with a co-average of 256. A minimum of ten spectra were collected across each sample, which were averaged and plotted for analysis. IR images/maps of the samples were collected in contact mode at a scan rate of 0.1 Hz with a co-average

of 16 using a silicon nitride cantilever with a nominal spring constant of  $0.5 \text{ Nm}^{-1}$  (EXC450 tips, AppNano, Mountain View, CA, USA). All spectral analyses were undertaken after normalization using GRAMS software (ThermoFisher, Waltham, MA, USA) and Analysis studio™ software (Anasys Instruments, USA). Spectral subtraction was used to show differences between the spectra of the samples. All the spectra collected from cell samples (ND treated, nanoshuttle treated, and control cell; Figure 3g) were processed in GRAMS software, smoothing was done with a polynomial function on 5 points. The spectra presented in Figure 5 were processed in the EssentialFTIR software package: using Savitzky golay smoothing with quadratic/cubic 25pt function. The endpoints were extrapolated then truncated. All subtractions were done by manually adjusting the subtraction factor applied to the epoxy spectrum. The subtraction factors used were different for each set of samples, but exactly the same subtraction factor was used within a given sample set. All subtractions were performed on smoothed spectra. Figure S4 were processed in Analysis studio software and smoothing was done using with a polynomial order of 2 on 25 points. Similarly spectra collected from FN-ND, non-adsorbed FN, and FN only (Figure 5) were processed in the Analysis studio software and smoothed in polynomial function of 2 and 5 points.

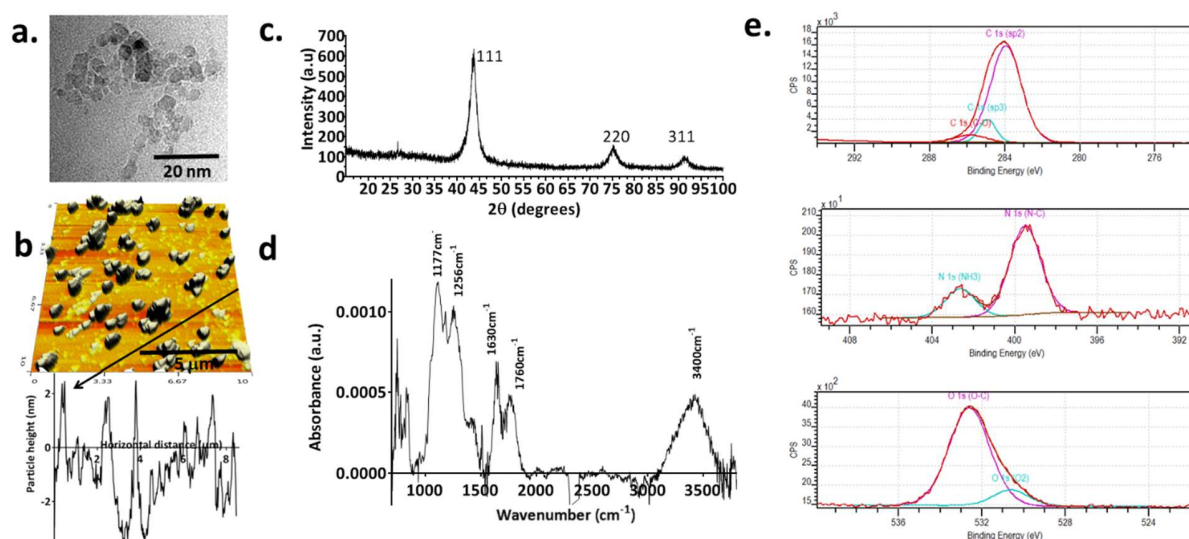


**Figure 2.** Physicochemical characterization of nanodiamond (ND). a) TEM image of ND particles showing the individual particles in the range of 4-5 nm with cuboidal shape; b) AFM height image of ND particles showing aggregates and individual nanoparticles; The profile analysis insert below the image show the height of the particles in the range of 4 nm; c) XRD graph showing key diamond peaks at  $2\theta$  of 111, 220 and 311. Grain size was determined to be around 4-5 nm; d) FTIR spectra collected from the bulk of ND indicated the presence of key diamond peaks in the region of 1117-1256  $\text{cm}^{-1}$ ; e) XPS spectra collected from NDs showed peaks related to carbon, oxygen and nitrogen. Elemental analysis showed 78.77% carbon, 8% oxygen and 1.7% of nitrogen.

## RESULTS AND DISCUSSION

**Physical properties;** XRD diffraction pattern of ND revealed diffraction maxima at the  $2\theta$  of 43.9 and 75.4, which correspond to diamond peaks<sup>52</sup>. The average grain size of diamond crystallites, estimated using the Scherrer formula, was 5 nm. The absence of non-diamond peaks and troughs in the spectra indicate high sample purity. TEM and AFM images of nanoparticles showed that they were cuboidal in shape and the size of individual particle was on average 3-5 nm, which was in agreement with the XRD results (Figure 2a, b and c).

**Chemical properties;** FTIR spectra collected from the bulk ND (Figure 2d) revealed typical ND peaks at 1107, 1177 and 1256  $\text{cm}^{-1}$ , which are due to stretching vibration of C-O group<sup>55</sup>. Low intensity peaks were observed at 1384  $\text{cm}^{-1}$  and 1436  $\text{cm}^{-1}$ , which are associated with aceto-group and C-H ( $\text{SP}_3$ ) bending vibration. Presence of aceto group may be due to contamination of ND during the laser assisted manufacturing stages<sup>55</sup>. Furthermore, the presence of a peak at 1760  $\text{cm}^{-1}$  (C=O) indicates that nanoparticles were partly oxidized, while the peak at 1630  $\text{cm}^{-1}$  correspond to the bending vibration of adsorbed water. The broad peak at 3400  $\text{cm}^{-1}$  corresponds to O-H stretching vibration. This indicates the adsorption of water on ND<sup>56,57</sup>.

XPS spectra showed clear ND peaks at 284, 285 and 287 eV binding energy. The peaks centred at 284 and 285.00 eV binding energy are due to the  $\text{sp}^2$  and  $\text{sp}^3$  hybridized carbon species respectively. Whereas the peaks centred at 286 and 287 eV binding energy is attributed to hydrogen containing groups (C-H) and oxygen bound carbon groups (C-O) respectively<sup>58</sup>. Elemental analysis from the high resolution spectra (Figure 2e) showed 78.77% carbon, 8% oxygen and 1.7% nitrogen content on the surface of ND. This indicated partial oxidation of the ND, which was in agreement with the FTIR result.

#### **Effect of ND on cell viability**

To select the concentration of ND to interrogate ND–protein interactions we evaluated *in vitro* cytotoxicity of ND using cells cultured in 2D monolayer. Cells were treated with ND at different concentrations (10, 25, 50 and 100  $\mu\text{g}.\text{mL}^{-1}$ ) for 48 h and metabolic activity of the cells, which corresponds to the viability of cells, was measured using CCK-8 assay. The measurement results showed no significant differences in viability of cell up to the concentration of 100  $\mu\text{g}.\text{mL}^{-1}$  for 48 h (Figure S2c). Extended incubation time (four days) resulted in the decrease of the viability with increasing concentration of ND, in particulate 25  $\mu\text{g}.\text{mL}^{-1}$  resulted in 24% drop of viability, while 50 and 100  $\mu\text{g}.\text{mL}^{-1}$  resulted respectively in 37% and 44% of cell viability drop (Figure S2c). In addition, cell viability was assessed in 3D (spheroids) using live/dead assay prior to ND–protein interaction studies. Result of live/dead assay showed that the majority of cells were viable within the spheroid at the concentration of 25  $\mu\text{g}.\text{mL}^{-1}$  (Figure S2b) and the diameter of the spheroid, which additionally indicates viability of cells in 3D culture<sup>54,59</sup> was similar to control sample. While the diameter increased (dilation of the spheroid that suggests drop of viability) increased for the higher concentrations of ND (Figure S2a). Based on both assays 25  $\mu\text{g}.\text{mL}^{-1}$  ND was selected as a concentration for which cells remain viable.

#### **Effect of ND on intracellular protein**

Since the development of AFM by Binnig *et. al.*<sup>60</sup>, this technique has been widely applied in nano and atomic scale imaging and probing with high spatial and temporal resolutions<sup>61,62</sup>. AFM-IR offers dual capability of scanning probe microscopy and nano scale IR spectroscopy, which is capable of detecting both nanochemical and nanomechanical characteristics. This technique is based on the localized thermal expansion of a sample after absorbing infrared light of a specific wavenumber. Thermally induced geometrical changes (at nanoscale) are detected by the deflection of the AFM cantilever that remains in contact with the sample. The measurement of these changes makes it possible to distinguish materials with different coefficient of thermal expansion (CTE). Because of the low CTE of ND ( $1.18 \times 10^{-6} \text{ K}^{-1}$ )<sup>63</sup>, it undergoes minimal expansion when exposed to the pulsed laser, which was confirmed by the AFM-IR spectra collected from pristine ND (Figure S3a). Taking advantage of the difference in CTE between ND and surrounding proteins ( $115 \times 10^{-6} \text{ K}^{-1}$ ), we can identify the NDs localized inside the treated cells.



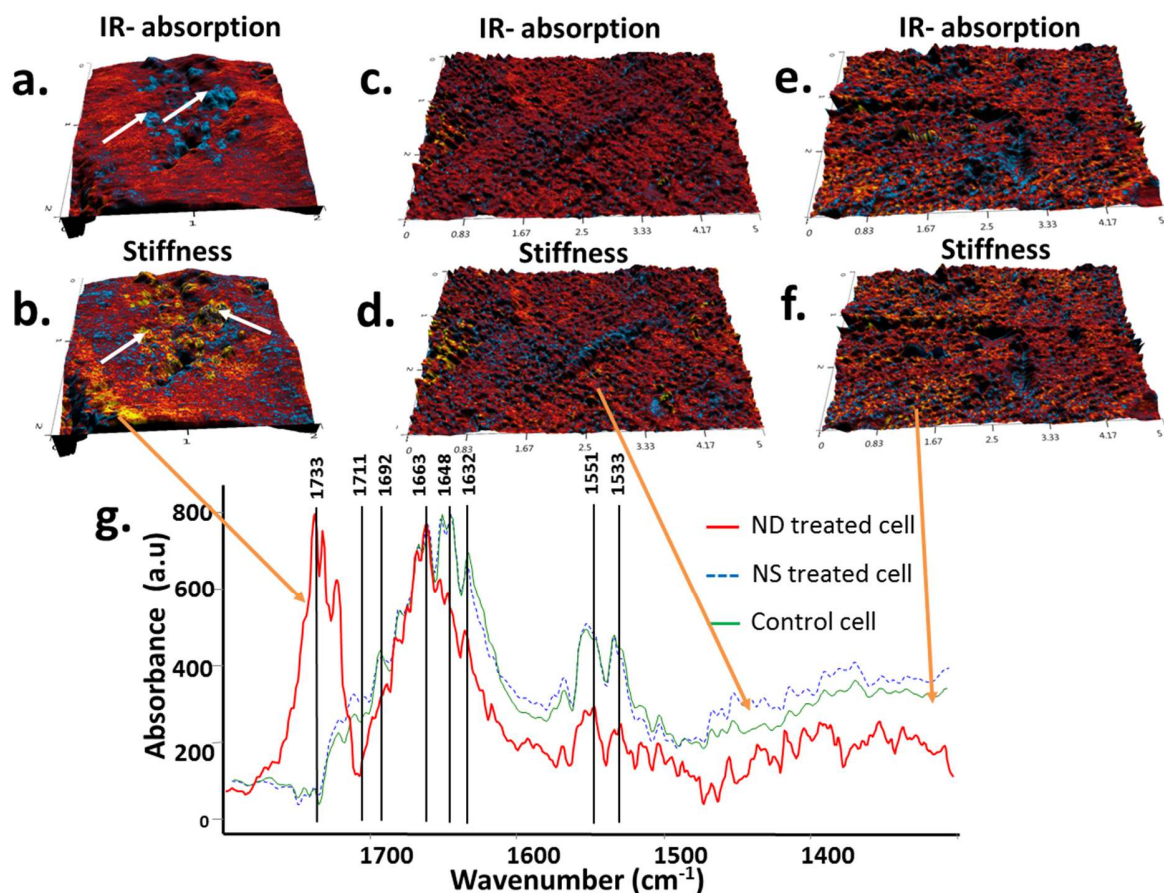


**Figure 3.** Topographical image, map of nanochemical and nanomechanical properties of a section of spheroid treated with nanodiamond, nanoshuttle and control cells. a) AFM-IR absorbance map of the ND treated spheroid section at  $1640\text{ cm}^{-1}$  showing inhomogeneous absorbance pattern, blue spots (white arrows) are the regions with lower absorbance (nanodiamond localised area) and red regions are the regions of higher absorbance (cellular region); b) corresponding nanomechanical map of ND- treated cell indicated that the region of lower absorbance at  $1640\text{ cm}^{-1}$  had higher stiffness (yellow spots, white arrows); d) nanomechanical map of nanoshuttle treated spheroid section; e) AFM-IR absorbance map of control cell section acquired at  $1640\text{ cm}^{-1}$ ; f) nanomechanical map of control cell; g) corresponding averaged AFM-IR spectra collected from ND treated cell, nanoshuttle treated and control cell section. All the spectra collected from individual samples were averaged, normalised and smoothed to 5 points with a polynomial function.



An absorbance map at  $1640\text{ cm}^{-1}$  was therefore collected across the ND treated, nanoshuttle treated and control cells (Figure 3a, 3c, 3e). The  $1640\text{ cm}^{-1}$  wave number was chosen to correspond with the amide I absorbance of proteins, maximising the contrast between the protein and ND. It was observed that there were regions of low absorbance only in the ND treated cells, which is preliminary evidence for the uptake of ND into the cell. Furthermore, the stiffness of the low absorbance region in the ND treated cell was also higher when compared to the surrounding cellular region (Figure 3a, 3b). These, combined with the similar cuboidal morphology of the NDs as determined by TEM and AFM confirms the uptake of ND in these cells. While, one could expect that these geometrical features and changes to IR amplitude could be associated with nanoshuttles that were used to levitate the cells, our control experiments on the nanoshuttle treated cells and cells only samples showed a lack of such features (Figure 3c and 3d). Furthermore, nanoshuttles are functionalised with poly-L-lysine and the AFM-IR spectra for nanoshuttle showed distinct peaks at  $1642\text{ cm}^{-1}$  for Poly-L-lysine (Figure S3b). If the features observed for ND treated samples were nanoshuttles then some absorbance signal at  $1640\text{ cm}^{-1}$  would have been apparent, which was not confirmed here. For the nanoshuttle treated samples, some region of higher stiffness were observed, however these zones had absorbance in  $1640\text{ cm}^{-1}$ , which excludes the existence of ND. Taken together, the presented results provide strong evidence that the cuboidal features detected for ND treated samples were associated with ND particles.

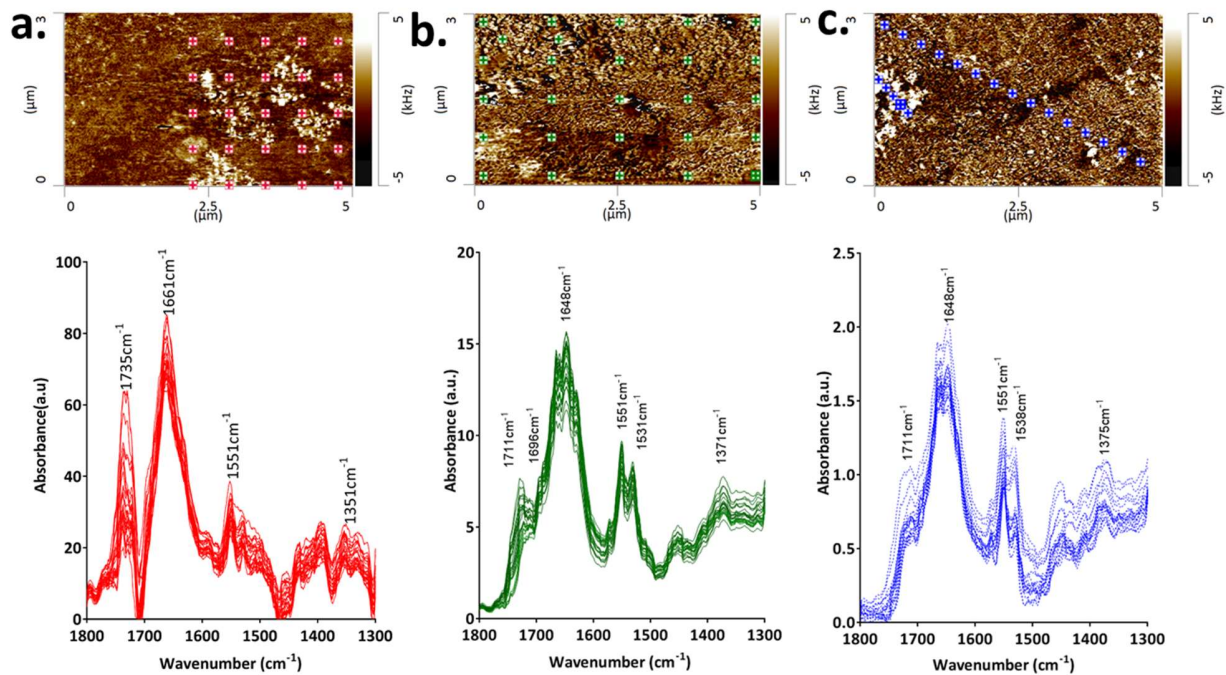


**Figure 4** a) AFM-IR array of spectra collected from nanodiamond treated Fao cells with corresponding frequency image. Amide I peak maxima was observed at  $1661\text{ cm}^{-1}$  indicating transition towards  $\beta$ -sheet content. Intensity of peak at  $1735\text{ cm}^{-1}$  was found to increase closer to the nanodiamond particle suggesting conformational changes in protein structure after the uptake of nanodiamond particle; b) AFM-IR array of spectra collected from nanoshuttle treated cells with corresponding frequency image; c) AFM-IR array of spectra collected from control cells with corresponding frequency image. Both the control and nanoshuttle treated cell had amide I maxima at  $1648\text{ cm}^{-1}$  indicating higher  $\alpha$ -helical content and peak at  $1735\text{ cm}^{-1}$  was not present.

Having confirmed the uptake of ND into the cells, the potential of ND in inducing protein conformational changes were investigated by collecting the AFM-IR spectra of the ND treated, nanoshuttle treated and control cells. Should the NDs induce any conformational changes, a change in the AFM-IR spectra should be expected. The averaged spectra recorded for ND-treated cells (Figure 3g) had an amide I absorption maxima at  $1663\text{ cm}^{-1}$  with a shoulder at  $1692\text{ cm}^{-1}$  (Figure 3g), indicating transition of protein conformation from  $\alpha$ -helical to the  $\beta$ -sheet and  $\beta$ -turn like structure<sup>36</sup>. On the contrary, both spectra for nanoshuttle treated cells and control cells (Figure 3g) had amide I absorption maxima at  $1648\text{ cm}^{-1}$ , depicting high alpha helical content. Further evidence for conformational changes in the protein structure can be found by comparing the ratio of the intensity of the amide I peak to the amide II peak. The amide I ( $1661\text{ cm}^{-1}$ ) to amide II ( $1551\text{ cm}^{-1}$ ) ratio of the ND treated cell is 2.64, while the ratio for the nanoshuttle and control cell ( $1648\text{ cm}^{-1}$ : $1551\text{ cm}^{-1}$ ) was 1.5-1.6. The change in this ratio was due to the reduction of amide II to amide I caused by ND induced oxidative stress<sup>23,24,25</sup>. The oxidative stress has been reported to result in carbonylation of intracellular proteins and cause aggregation, conformational change and even total loss of protein functionality<sup>64</sup>. This process has been observed in Hela human cervical cancer cells treated with ND manufactured by detonation techniques<sup>65</sup>.

In addition, a high intensity peak at  $1733\text{ cm}^{-1}$  was observed in the ND treated cell which is not as pronounce in both nanoshuttle treated and control cells. The increased intensity of this peak suggests the protonation of  $-\text{COO}^-$  group in the proteins (Figure 4a, 4b, 4c). The observed protonation may be due to two processes. Firstly, it may be the result of protein denaturation causing a change in pKa near the ND-protein interface. Alternatively, it may occur also due to the direct interaction between the protein and substrate with low dielectric permittivity. The ND's low dielectric permittivity ( $\epsilon$ ) of 8.7<sup>66</sup> could potentially lead to a shift of the carboxyl group's dissociation equilibrium toward the neutral protonated species. However, without further study, it is uncertain whether protein denaturation or direct ND interaction, or a combination of both, is responsible for the protonation.

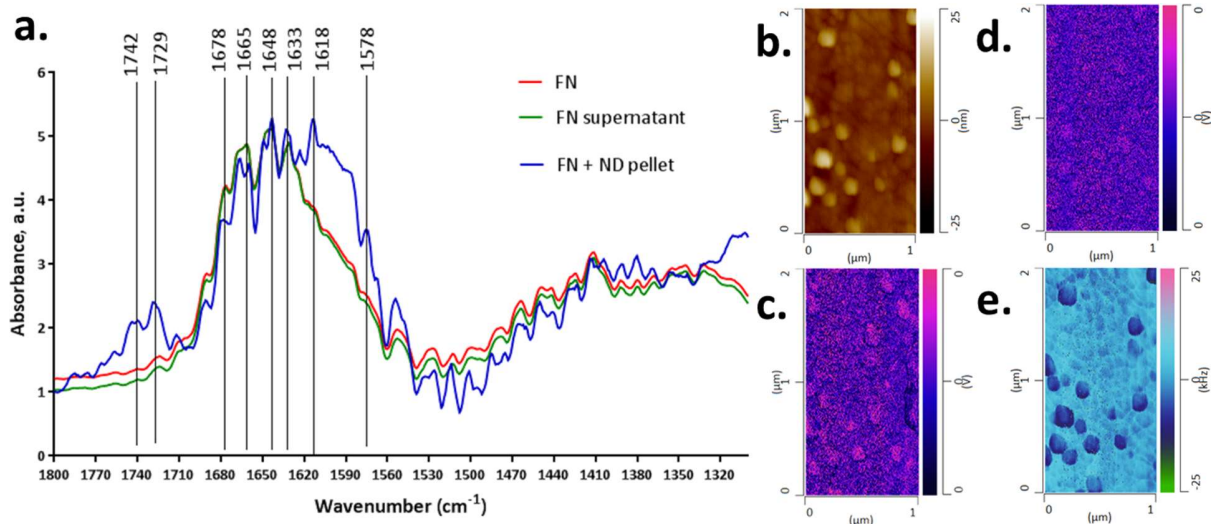


**Figure 5:** Topographical image, map of nano-mechanics and chemistry of conformational changes induced due to adsorption of fibronectin on nanodiamond. a) AFM-IR spectra collected from pure fibronectin (FN), non-adsorbed fibronectin (FN supernatant), and adsorbed protein (FN+ND pellet). Clear differences in the spectra was observed with broadening of spectra in amide I region in case of adsorbed protein with the main peak at  $1618\text{ cm}^{-1}$  and additional peak was observed at

1729  $\text{cm}^{-1}$  indicating conformational changes in the protein; b) height image showing cuboidal nanodiamond particles with aggregates of FN; c) absorbance map acquired from FN-ND sample at 1620  $\text{cm}^{-1}$  showed bright pink spots on these features indicating the regions where denaturation and conformational changes occurred in FN after adsorption to ND; d) absorbance map at 1723  $\text{cm}^{-1}$  shows zones of absorbance (bright pink regions) suggesting possible sites where protonation of FN occurred; e) Stiffness map indicated localised softness (dark blue spots) due to the adsorption of protein on these particles.

**Nanodiamond- extracellular protein interaction.** To confirm the impact of ND on extracellular proteins, fibronectin was similarly investigated for conformational changes using the AFM-IR. FN is present in plasma as well as the cell surface and is secreted primarily by liver hepatocytes. It plays a key role in cell proliferation, migration, wound healing and is involved in the opsonisation of nanoparticles<sup>67,68</sup>. FN is also known to be susceptible to conformational changes after adsorption to a substrate, which makes this protein an ideal model to study ND-protein interactions.

AFM-IR spectra were collected from FN adsorbed to ND (FN-ND), FN -supernatant, and FN. Much like the previous case with Fao cells, conformational changes should alter the AFM-IR spectra. The spectra from all three samples had three peaks in common, the amide I peaks at 1633  $\text{cm}^{-1}$  and 1648  $\text{cm}^{-1}$ , along with a shoulder peak at 1678  $\text{cm}^{-1}$  (Figure 5a). All these peaks correspond to high  $\beta$ -sheet and  $\beta$ -turn components within the secondary structure of FN<sup>69</sup>. This is in agreement with the literature where FN has been reported to have majority of secondary protein structure in the  $\beta$ -strand conformations<sup>70</sup>. However, when FN is adsorbed to NDs (FN-ND), an additional amide I peak with absorption maxima at 1618  $\text{cm}^{-1}$  was observed which was not evident in the FN-supernatant and FN control samples (Figure 5a). The appearance of such a peak is associated with the multimerization and aggregation of proteins<sup>71</sup>. In the case of FN, the aggregation occurs due to intermolecular hydrogen bonding, ultimately leading to intermolecular  $\beta$ -sheet formation<sup>71</sup>. The initial hydrogen bonding between monomeric FN is only possible if the FN undergoes denaturation as a result of adsorption to ND. This findings is in agreement with the study where temperature induced denaturation of FN resulted in the formation of FN aggregates<sup>71</sup>.

Additionally, the appearance of a prominent peak at 1729  $\text{cm}^{-1}$  in case of FN-ND sample indicates protonation of  $\text{COO}^-$  in the FN structure as seen in ND treated cells, which confirms the conformational changes and possible denaturation of the FN<sup>69,72,73</sup>.

In order to identify the location of conformational change, absorbance maps were collected for FN-ND at wave numbers 1620  $\text{cm}^{-1}$  (Figure 5b) and 1723  $\text{cm}^{-1}$  (Figure 5c). The absorbance maps clearly demonstrate zones of higher absorbance (bright pink spots), indicating where conformational changes in FN occurred after adsorption. These zones were characterised by a cuboidal morphology and had lower mechanical stiffness compared to its surrounding (Figure 5 c), suggesting that the ND was coated by FN. When an array of spectra were collected from the FN-ND samples, the intensity of the peak at 1725  $\text{cm}^{-1}$  was more pronounced closer to the ND particle (Figure S4). This result further confirms that conformational changes and denaturation occurs near the FN-ND interface.

Cumulatively our results evidenced that ND can induce conformational changes in the secondary structure of both intra- and extracellular protein structures. Our results highlighted that ND caused conformational changes and/or denaturation of proteins in its immediate vicinity. These effects may result in the total loss of functionality of the protein at a cellular level and thus may have a negative effect on cell viability and vitality.

## CONCLUSION

The high spatial resolution (<20 nm) of AFM-IR has enabled the study of both intra and extracellular protein interactions with individual nanoparticles. For the first time, the interface of internalized nanoparticles was examined using AFM-IR and we demonstrated that proteins, both intracellular and extracellular, undergo conformational changes at the ND-protein interface. These results suggest that individual nanoparticles have negative effects on the protein structure. The high resolution nanoscale information on nanoparticle–protein interaction generated using the AFM-IR technique have powerful implication for our understanding of nanomaterials toxicity in bodily environment.

## ACKNOWLEDGMENT

This work was supported by EU Horizon 2020 MSCA-RISE grant (Project 690945 “Carbon-based nanomaterials for theranostic application”) which is gratefully acknowledged.

## REFERENCES

- (1) Alhaddad, A.; Adam, M. P.; Botsoa, J.; Dantelle, G.; Perruchas, S.; Gacoin, T.; Mansuy, C.; Lavielle, S.; Malvy, C.; Treussart, F. *Small* **2011**, *7*, 3087-3095.
- (2) Chow, E. K.-H.; Ho, D. *Sci. Transl. Med.* **2013**, *5*, 216rv214-216rv214.
- (3) Kaur, R.; Badea, I. *Int. J. Nanomedicine* **2013**, *8*, 203.
- (4) Wagstaff, A. J.; Brown, S. D.; Holden, M. R.; Craig, G. E.; Plumb, J. A.; Brown, R. E.; Schreiter, N.; Chrzanowski, W.; Wheate, N. J. *Inorg. Chim. Acta* **2012**, *393*, 328-333.
- (5) Baek, S.; Singh, R. K.; Khanal, D.; Patel, K. D.; Lee, E.-J.; Leong, K. W.; Chrzanowski, W.; Kim, H.-W. *Nanoscale* **2015**, *7*, 14191-14216.
- (6) Vijayanthimala, V.; Tzeng, Y.-K.; Chang, H.-C.; Li, C.-L. *Nanotechnology* **2009**, *20*, 425103.
- (7) Forest, V.; Cottier, M.; Pourchez, J. *Nano Today* **2015**.
- (8) Zhang, S.; Gao, H.; Bao, G. *ACS nano* **2015**, *9*, 8655-8671.
- (9) Zhang, X.; Hu, W.; Li, J.; Tao, L.; Wei, Y. *Toxicology Research* **2012**, *1*, 62-68.
- (10) Chithrani, B. D.; Chan, W. C. *Nano Lett.* **2007**, *7*, 1542-1550.
- (11) Chithrani, B. D.; Ghazani, A. A.; Chan, W. C. *Nano Lett.* **2006**, *6*, 662-668.
- (12) Chu, Z.; Miu, K.; Lung, P.; Zhang, S.; Zhao, S.; Chang, H.-C.; Lin, G.; Li, Q. *Sci. Rep.* **2015**, *5*.
- (13) Favi, P. M.; Gao, M.; Johana Sepúlveda Arango, L.; Ospina, S. P.; Morales, M.; Pavon, J. J.; Webster, T. J. *Journal of Biomedical Materials Research Part A* **2015**.
- (14) Chowdhury, S. M.; Lalwani, G.; Zhang, K.; Yang, J. Y.; Neville, K.; Sitharaman, B. *Biomaterials* **2013**, *34*, 283-293.
- (15) Zeng, K.; Li, J.; Zhang, Z.; Yan, M.; Liao, Y.; Zhang, X.; Zhao, C. *Journal of Materials Chemistry B* **2015**.
- (16) Wu, Y.; Tang, W.; Wang, P.; Liu, C.; Yuan, Y.; Qian, J. *Particle & Particle Systems Characterization* **2015**.
- (17) Roach, P.; Farrar, D.; Perry, C. C. *J. Am. Chem. Soc.* **2006**, *128*, 3939-3945.
- (18) Lynch, I.; Dawson, K. A. *Nano Today* **2008**, *3*, 40-47.

- (19) Elsaesser, A.; Howard, C. V. *Advanced drug delivery reviews* **2012**, *64*, 129-137.
- (20) Shen, X.-C.; Liou, X.-Y.; Ye, L.-P.; Liang, H.; Wang, Z.-Y. *J. Colloid Interface Sci.* **2007**, *311*, 400-406.
- (21) Shang, L.; Wang, Y.; Jiang, J.; Dong, S. *Langmuir* **2007**, *23*, 2714-2721.
- (22) Fei, L.; Perrett, S. *Int. J. Mol. Sci.* **2009**, *10*, 646-655.
- (23) Li, J.; Strong, R.; Trevisan, J.; Fogarty, S. W.; Fullwood, N. J.; Jones, K. C.; Martin, F. L. *Environ. Sci. Technol.* **2013**, *47*, 10005-10011.
- (24) Li, J.; Ying, G.-G.; Jones, K. C.; Martin, F. L. *Analyst* **2015**, *140*, 2687-2695.
- (25) Li, J.; Tian, M.; Cui, L.; Dwyer, J.; Fullwood, N. J.; Shen, H.; Martin, F. L. *Sci. Rep.* **2016**, *6*.
- (26) Perevedentseva, E.; Cai, P.-J.; Chiu, Y.-C.; Cheng, C.-L. *Langmuir* **2010**, *27*, 1085-1091.
- (27) Perevedentseva, E.; Tu, J.; Cheng, C.; Chung, P.; Chang, H.; Cheng, C. *Nanotechnology* **2006**, *2*, 440-443.
- (28) Wang, H.-D.; Niu, C. H.; Yang, Q.; Badea, I. *Nanotechnology* **2011**, *22*, 145703.
- (29) Downes, A.; Mouras, R.; Elfick, A. *BioMed Research International* **2010**, *2010*.
- (30) Centrone, A. *Annu. Rev. Anal. Chem.* **2015**.
- (31) Gruszecki, W.; Kulik, A.; Janik, E.; Bednarska, J.; Luchowski, R.; Grudzinski, W.; Dietler, G. *Nanoscale* **2015**, *7*, 14659-14662.
- (32) Dazzi, A.; Prazeres, R.; Glotin, F.; Ortega, J. *Opt. Lett.* **2005**, *30*, 2388-2390.
- (33) Dazzi, A.; Prazeres, R.; Glotin, F.; Ortega, J. *Ultramicroscopy* **2007**, *107*, 1194-1200.
- (34) Dazzi, A.; Prazeres, R.; Glotin, F.; Ortega, J. *Infrared physics & technology* **2006**, *49*, 113-121.
- (35) Katzenmeyer, A. M.; Holland, G.; Kjoller, K.; Centrone, A. *Anal. Chem.* **2015**, *87*, 3154-3159.
- (36) Ruggeri, F.; Longo, G.; Faggiano, S.; Lipiec, E.; Pastore, A.; Dietler, G. *Nat. Commun.* **2015**, *6*.
- (37) Krueger, A. *Journal of Materials Chemistry* **2008**, *18*, 1485-1492.
- (38) Mochalin, V. N.; Shenderova, O.; Ho, D.; Gogotsi, Y. *Nature Nanotechnology* **2012**, *7*, 11-23.
- (39) Schrand, A. M.; Hens, S. A. C.; Shenderova, O. A. *Critical reviews in solid state and materials sciences* **2009**, *34*, 18-74.
- (40) Manus, L. M.; Mastarone, D. J.; Waters, E. A.; Zhang, X.-Q.; Schultz-Sikma, E. A.; MacRenaris, K. W.; Ho, D.; Meade, T. J. *Nano letters* **2009**, *10*, 484-489.
- (41) Spitsyn, B.; Denisov, S.; Skorik, N.; Chopurova, A.; Parkaeva, S.; Belyakova, L.; Larionov, O. *Diamond and Related Materials* **2010**, *19*, 123-127.
- (42) Nesterenko, P. N.; Fedyanina, O. N.; Volgin, Y. V.; Jones, P. *Journal of Chromatography A* **2007**, *1155*, 2-7.
- (43) Wu, C. C.; Han, C. C.; Chang, H. C. *Journal of the Chinese Chemical Society* **2010**, *57*, 583-594.
- (44) Chou, C.-C.; Lee, S.-H. *Wear* **2010**, *269*, 757-762.
- (45) Zhang, Q.; Mochalin, V. N.; Neitzel, I.; Hazeli, K.; Niu, J.; Kotsos, A.; Zhou, J. G.; Lelkes, P. I.; Gogotsi, Y. *Biomaterials* **2012**, *33*, 5067-5075.
- (46) Luo, X.; Zhang, H.; Cao, Z.; Cai, N.; Xue, Y.; Yu, F. *Carbohydrate Polymers* **2016**, *143*, 231-238.
- (47) Brady, M. A.; Renzing, A.; Douglas, T. E.; Liu, Q.; Wille, S.; Parizek, M.; Bacakova, L.; Kromka, A.; Jarosova, M.; Godier, G. *Journal of nanoscience and nanotechnology* **2015**, *15*, 1060-1069.
- (48) Souza, G. R.; Molina, J. R.; Raphael, R. M.; Ozawa, M. G.; Stark, D. J.; Levin, C. S.; Bronk, L. F.; Ananta, J. S.; Mandelin, J.; Georgescu, M.-M. *Nature nanotechnology* **2010**, *5*, 291-296.
- (49) Wang, D.; Tong, Y.; Li, Y.; Tian, Z.; Cao, R.; Yang, B. *Diamond and Related Materials* **2013**, *36*, 26-34.
- (50) Zhao, L.; Xu, Y.-H.; Akasaka, T.; Abe, S.; Komatsu, N.; Watari, F.; Chen, X. *Biomaterials* **2014**, *35*, 5393-5406.
- (51) Svetlakov, A. S.; Brandt, N. N.; Priezzhev, A. V.; Chikishev, A. Y. *J. Biomed. Opt.* **2015**, *20*, 047004-047004.
- (52) Zousman, B.; Levinson, O. In *Nanodiamond*; The Royal Society of Chemistry, 2014, pp 112-127.
- (53) Timm, D. M.; Chen, J.; Sing, D.; Gage, J. A.; Haisler, W. L.; Neeley, S. K.; Raphael, R. M.; Dehghani, M.; Rosenblatt, K. P.; Killian, T. *Sci. Rep.* **2013**, *3*, 1-8.

- (54) Hau, H.; Khanal, D.; Rogers, L.; Suchowerska, N.; Kumar, R.; Sridhar, S.; McKenzie, D.; Chrzanowski, W. *Bioengineering & Translational Medicine* **2016**.
- (55) Baidakova, M.; Kukushkina, Y. A.; Sitnikova, A.; Yagovkina, M.; Kirilenko, D.; Sokolov, V.; Shestakov, M.; Vul, A. Y.; Zousman, B.; Levinson, O. *Physics of the Solid State* **2013**, *55*, 1747-1753.
- (56) Pohl, A.; Joch, S.; Michael, J.; Boschke, E.; Quenzel, P.; Schreiber, J.; Lapina, V.; Opitz, J. In *European Conference on Biomedical Optics*; Optical Society of America, 2011, p 80871T.
- (57) Wen, C.; Jin, Z.; Liu, X.; Li, X.; Guan, J.; Sun, D.; Lin, Y.; Tang, S.; Zhou, G.; Lin, J. *Guang pu xue yu guang pu fen xi= Guang pu* **2005**, *25*, 681-684.
- (58) Xie, F.; Xie, W.; Gong, L.; Zhang, W.; Chen, S.; Zhang, Q.; Chen, J. *Surf. Interface Anal.* **2010**, *42*, 1514-1518.
- (59) Timm, D. M.; Chen, J.; Sing, D.; Gage, J. A.; Haisler, W. L.; Neeley, S. K.; Raphael, R. M.; Dehghani, M.; Rosenblatt, K. P.; Killian, T. *Sci. Rep.* **2013**, *3*.
- (60) Binnig, G.; Quate, C. F.; Gerber, C. *Phys. Rev. Lett.* **1986**, *56*, 930.
- (61) Chrzanowski, W.; Lee, J. H.; Kondyurin, A.; Lord, M. S.; Jang, J. H.; Kim, H. W.; Bilek, M. M. *Adv. Funct. Mater.* **2015**, *25*, 339-339.
- (62) Haghi, M.; Traini, D.; Wood, L. G.; Oliver, B.; Young, P. M.; Chrzanowski, W. *Journal of Materials Chemistry B* **2015**, *3*, 2583-2589.
- (63) Kidalov, S. V.; Shakhov, F. M. *Materials* **2009**, *2*, 2467-2495.
- (64) Castro, J. P.; Ott, C.; Jung, T.; Grune, T.; Almeida, H. *Free Radic. Biol. Med.* **2012**, *53*, 916-925.
- (65) Mytych, J.; Lewinska, A.; Bielak-Zmijewska, A.; Grabowska, W.; Zebrowski, J.; Wnuk, M. *Chem. Biol. Interact.* **2014**, *220*, 51-63.
- (66) Batsanov, S. S.; Gavrilkin, S. M.; Batsanov, A. S.; Poyarkov, K. B.; Kulakova, I. I.; Johnson, D. W.; Mendis, B. G. *J. Mater. Chem.* **2012**, *22*, 11166-11172.
- (67) Mosher, D. F.; Furcht, L. T. *J. Invest. Dermatol.* **1981**, *77*, 175-180.
- (68) Pankov, R.; Yamada, K. M. *J. Cell Sci.* **2002**, *115*, 3861-3863.
- (69) Michael, K. E.; Vernekar, V. N.; Keselowsky, B. G.; Meredith, J. C.; Latour, R. A.; García, A. J. *Langmuir* **2003**, *19*, 8033-8040.
- (70) Patel, S.; Chaffotte, A. F.; Amana, B.; Goubard, F.; Pauthe, E. *The international journal of biochemistry & cell biology* **2006**, *38*, 1547-1560.
- (71) Pauthe, E.; Pelta, J.; Patel, S.; Lairez, D.; Goubard, F. *Biochimica et Biophysica Acta (BBA)-Protein Structure and Molecular Enzymology* **2002**, *1597*, 12-21.
- (72) Giroux, T. A.; Cooper, S. L. *J. Colloid Interface Sci.* **1990**, *139*, 351-362.
- (73) Halter, M.; Antia, M.; Vogel, V. *J. Control. Release* **2005**, *101*, 209-222.